

RME-GAN: A Learning Framework for Radio Map Estimation Based on Conditional Generative Adversarial Network

Songyang Zhang^{ID}, Achintha Wijesinghe^{ID}, and Zhi Ding^{ID}, *Fellow, IEEE*

Abstract—Outdoor radio coverage map estimation is an important tool for network planning and resource management in modern Internet of Things (IoT) and cellular systems. A radio map spatially describes radio signal strength distribution and provides network coverage information. A practical problem is to estimate fine-resolution radio maps from sparse radio strength measurements. However, nonuniformly positioned measurements and access constraints pose challenges to accurate radio map estimation (RME) and spectrum planning in many outdoor environments. In this work, we develop a two-phase learning framework for RME by integrating well-known radio propagation model and designing a conditional generative adversarial network (cGAN). We first explore global information to extract radio propagation patterns. Next, we focus on the local features to estimate the shadowing effect on radio maps in order to train and optimize the cGAN. Our experimental results demonstrate the efficacy of the proposed framework for RME based on generative models from sparse observations in outdoor scenarios.

Index Terms—Conditional generative adversarial networks (cGANs), network planning, radio map estimation (RME), radio measurement.

I. INTRODUCTION

THE RELENTLESS advances of information technologies have spawned many novel concepts and applications, such as the Internet of Things (IoT), autonomous driving, and cellular networks. For these wireless services, efficient spectrum planning and network coverage analysis are critical to spectrum efficiency and user experience. Specifically, radio maps provide vital information on the spatial distribution of radio frequency (RF) signal power, and facilitate resource allocation and network outage diagnosis [1]. In general, RF “radio map” refers to a geographical signal power spectrum density (PSD), formed by cumulative received RF signal power, as a function of spatial locations and frequencies, and may also exhibit temporal variations [2]. Capturing rich information on propagation behavior and spectrum occupancy, radio maps could provide detailed spatial information on

Manuscript received 5 April 2023; accepted 15 May 2023. Date of publication 19 May 2023; date of current version 9 October 2023. This work was supported in part by the National Science Foundation under Grant 2029848 and Grant 2029027. Songyang Zhang and Achintha Wijesinghe contributed equally to this work. (Corresponding author: Zhi Ding.)

The authors are with the Department of Electrical and Computer Engineering, University of California at Davis, Davis, CA 95616 USA (e-mail: sydzheng@ucdavis.edu; achwijesinghe@ucdavis.edu; zdng@ucdavis.edu).

Digital Object Identifier 10.1109/JIOT.2023.3278235

radio PSD distribution [3], shown in Fig. 1(a). Consequently, many radio-map-assisted applications have been made possible for IoT intelligence and wireless resource allocation as shown in Fig. 1(c), including 3-D path planning for cellularly connected unmanned aerial vehicle (UAV) [4], radio-based resource allocation for autonomous driving [5], environment map reconstruction from radio maps [6], and fault diagnosis in cyber-physical systems [7]. However, practical RF signal power measurements are mostly sparsely sampled by distributed sensors or user devices as shown in Fig. 1(b). Thus, to better leverage radio maps in network optimization, planning, and resource allocation in IoT and wireless systems, we aim to overcome the practical challenge of reconstructing fine-resolution radio maps from sparse and irregularly distributed observations. Our goal in this work is to develop a data-driven approach for more efficient and accurate estimation of radio maps from sparse observations for IoT and wireless resource management.

Most current approaches to radio map estimation (RME) (reconstruction) can be categorized into either model based or model-free. Model-based methods usually assume certain signal propagation models and express the received signal PSD as a combination from active transmitters [2]. For example, Lee and Han [8] introduced the log-distance path-loss (LDPL) model for Wi-Fi radio map reconstruction. In [9], another model-based method proposed interpolation based on thin-plate splines kernels. On the other hand, model-free methods do not assume a specific model but explore more neighborhood information. Typical examples include radial basis function (RBF) [10] interpolation and inverse distance weighted (IDW) interpolation [11]. In addition to interpolation methods, there have also been a number of works that apply machine learning for radio map reconstruction. Levie et al. [12] presented a fast RME based on Unet [13]. Another team [14] proposed deep auto-encoders (AE) for estimating geographical PSD distribution. We will provide a more complete literature review later in Section II.

Despite many successes, existing solutions still exhibit certain limitations. First, unlike the problem of astronomical image analysis [15] and 3-D city map reconstruction [16], ground truth radio map is more sensitive to the complex environment beyond mere radio propagation models. Failure to capture effects from shadowing or obstacles limits the efficacy of model-based approaches. On the other hand, the performance of model-free methods relies on

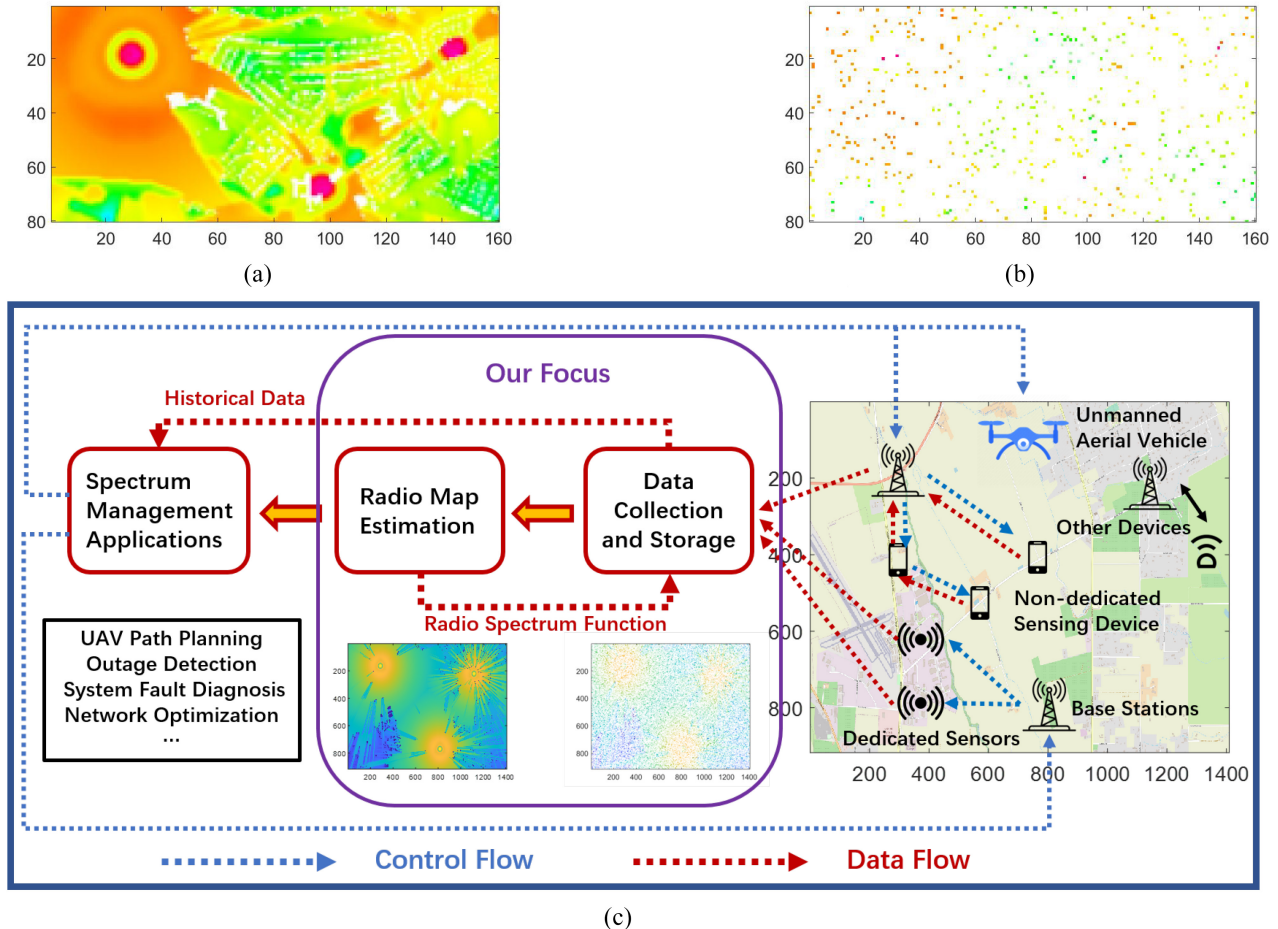


Fig. 1. Example of radio map: (a) radio map generated from simulators with three transmitters; (b) 1000 samples from the original radio map; and (c) illustration of background, where our focus is to develop data-driven approaches for radio map reconstruction in IoT management and wireless spectrum optimization.

the quality of observed samples. Generally, they assume a uniform distribution of measurements over the geometric space. However, in practical applications such as minimization of drive test (MDT) [17], measurements are collected from user devices, which are typically nonuniformly distributed within cell coverage. It is a challenge to process unevenly distributed observations efficiently. Moreover, samples in different training sets do not necessarily have the same radio propagation models and parameters. In view of their respective strengths and shortcomings, we should consider the effective integration of model-based and model-free methods.

To address the aforementioned problems, we investigate radio propagation in the outdoor scenario and propose a two-phase learning framework (RME-GAN) for RME based on conditional generative adversarial networks (cGANs) [18]. Since a radio map can be dynamically constructed from real-time measures and continuously updated [2], we mainly focus on the step of RME from sparse observations over geographical locations. In Phase 1, we integrate learning-based and model-based principles to extract global information while leveraging the radio propagation model. In Phase 2, we utilize different sampling strategies to capture local radio map features and explore the shadowing effect. More specifically, we propose to capture the sharp features in the Fourier domain for

detailed information, before resampling the measured signals geometrically to address the nonuniformity among distributed observations. We summarize our contributions as follows.

- 1) We introduce a novel strategy to integrate well-known radio propagation models into popular data-driven learning approaches to guide learning machines toward global radio map information in the first phase of our proposed framework.
- 2) We design new sampling strategies to capture local radio information and shadowing effects in radio propagation to accommodate irregularly distributed practical observations in the second phase of the proposed framework.
- 3) We provide comprehensive experimental comparisons with state-of-the-art methods in terms of both reconstruction accuracy and fault diagnosis.

Our experimental results demonstrate the strength of our proposed strategies in capturing both global model information and local shadowing features, as well as the power of the two-phase learning framework in radio map reconstruction, thereby facilitating radio-map-assisted resource management for IoT and wireless systems.

We organize the remainder of this work as follows. We first overview the related works of radio map reconstruction and generative adversarial network (GAN) models in Section II.

We then introduce our problem formulation in Section III. In Section IV, we present the details of the proposed two-phase learning frameworks based on cGAN. Following the presentation of the experimental results in Section V, we conclude our works in Section VI.

II. RELATED WORK

In this section, we provide an overview of RME from sparse samples based on either model-based or model-free approaches. We also introduce GAN models.

A. Radio Map Estimation

1) *Model-Based Radio Map Estimation*: Model-based approaches usually leverage a certain signal propagation model. Specifically, a radio map function is modeled as a function of frequency f and a geographic location \mathbf{c} by

$$\Phi(\mathbf{c}, f) = \sum_{i=1}^{N_t} g_i(\mathbf{c}, f) \Psi_i(f) \quad (1)$$

where N_t denotes the number of transmitters, g_i denotes the channel power gain of the i th transmitter, and $\Psi_i(f)$ is the PSD of the i th transmission [2]. Here, g_i can either be assumed as an explicit function with prior knowledge depending on specific tasks or be represented in terms of sensor parameters. For example, Lee and Han [8] modeled a single narrowband Wi-Fi transmitter with g_i according to the LDPL model. Bazerque et al. [9] modeled g_i as a kernel expansion to estimate the power gain. Other model-based methods include parallel factor analysis (PARAFAC) [19] and fixed rank Kriging [20].

2) *Model-Free Radio Map Reconstruction*: Different from model-based methods, model-free methods usually do not assume a specific propagation model but favor neighborhood information. In general, the model-free methods can be categorized as interpolation-based methods and learning-based methods as follows.

1) *Interpolation-Based Methods*: Interpolation-based approaches express the PSD at a particular location as a combination of neighborhood measurements, i.e.,

$$\Phi(\mathbf{c}, f) = \sum_{i=1}^{N_s} w_i(\mathbf{c}, f) q_i(f) \quad (2)$$

where q_i denotes the observation from the i th observation and w_i is the combination weight [2]. One typical example is IDW interpolation [11], where the power gain is inversely proportional to the distance between transmitters and receivers. Besides linear interpolation, an effective alternative is RBF interpolation [10], where different kernels, such as Gaussian, multi quadrics, or spline, can be applied. Another classic interpolation approach is ordinary Kriging methods [21], where the PSD is optimized by minimizing the variance of estimation error. Beyond these traditional methods, recent works of radio map interpolation studied integration with novel data analysis concepts, such as graph signal processing [22], crowdsourcing methods [23], image inpainting [7], [24], and tensor completion [25].

2) *Learning-Based Methods*: Recent applications and success of machine learning in wireless networks and IoT intelligence have stimulated more interests in learning-based RME as another promising direction. Different from explicit interpolation, learning-based methods focus on finding a direct mapping from an input geometric map to its output PSD measurement. The functional relationship between input and output is usually captured by a neural network. For example, Unet is introduced in [12] for predicting path loss. Similarly, the deep AE is another design for deep neural network mapping [14]. Other learning frameworks for RME include transfer learning [26], GAN [27], [28], [29], deep Gaussian process [30], reinforcement learning [31], and deep neural networks [32], [33], [34]. Interested readers could refer to [35] for a more thorough overview of data-driven radio map reconstruction.

B. Generative Adversarial Networks

The idea of GANs to study a collection of training examples to acquire sufficient information on sample distribution in order to generate data samples with similar distribution [36]. In GAN, two neural networks interact in the form of a zero-sum game, in which the generator G aims to generate new data with the same statistics as the training data set while the discriminator D focuses on the identification of the true and fake data samples. Suppose the generator learns the distribution p_g over data \mathbf{x} by mapping a prior noise distribution $p_z(\mathbf{z})$ to data space. The GAN model can be trained via

$$\min_G \max_D V(D, G) = \mathbb{E}_{\mathbf{x} \sim p_{\text{data}}(\mathbf{x})} [\log D(\mathbf{x})] + \mathbb{E}_{\mathbf{z} \sim p_z(\mathbf{z})} [\log(1 - D(G(\mathbf{z})))] \quad (3)$$

where $\mathbb{E}[\cdot]$ refers to the expectation operation.

With the development of machine learning, GAN can be extended to a conditional model (cGAN) if the generator and discriminator are conditioned on some extra information \mathbf{I} [18]. Then, the objective function could be set as

$$\min_G \max_D V(D, G) = \mathbb{E}_{\mathbf{x} \sim p_{\text{data}}(\mathbf{x})} [\log D(\mathbf{x}|\mathbf{I})] + \mathbb{E}_{\mathbf{z} \sim p_z(\mathbf{z})} [\log(1 - D(G(\mathbf{z}|\mathbf{I})))]. \quad (4)$$

Note that, previous works have shown that cGAN can be customized to learn the desired properties by mixing the traditional loss function with cGAN objectives [37] and utilizing the corresponding feature vectors as input. See the illustration in Fig. 2. For example, to generate a painted image from a sketch, one can input the sketch to the generator and formulate the training process as a one-to-one mapping. No random noise vector should be involved in such a mapping problem. The customized cGAN frameworks have achieved success in applications, including image painting [38], image-to-image translation [39], and image manipulation [40].

III. PROBLEM FORMULATION

Now, we present the problem formulation in this work. In general, we focus on the radio map reconstruction from sparse observations in the outdoor scenario.

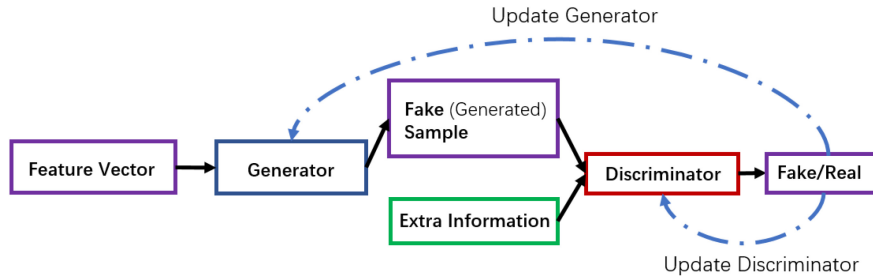


Fig. 2. Example of a customized cGAN.

Our model considers a set of regions with sparse observations of network coverage, similar to Fig. 1(b). Each region is conformed to a size of 256×256 grid and contains N_t transmitters with known positions. Let $\mathbf{P}_{ti} \in \mathbb{R}^{N_t \times 2}$ denote the 2-D coordinates of transmitters for the i th region. Region i is also attributed with their corresponding urban maps $\mathbf{m}_i \in \mathbb{R}^{256 \times 256}$ with building information. Instead of knowing the fine-resolution radio map of the whole space, each region only observes a set of K_i sparse samples $(\mathbf{x}_i, \mathbf{c}_i)$ collected from sensors, where $K_i \leq 256 \times 256$, $\mathbf{x}_i \in \mathbb{R}_+^{K_i}$ are the nonnegative observed PSD, and $\mathbf{c}_i \in \mathbb{R}^{K_i \times 2}$ are the 2-D coordinates of the corresponding observations. Thus, each region i is characterized by

$$\mathcal{F}_i = \{(\mathbf{x}_i, \mathbf{c}_i), \mathbf{m}_i, \mathbf{P}_{ti}\}. \quad (5)$$

Suppose that some regions have the ground truth of the fine-resolution radio map \mathbf{y} . Treating these regions as training regions, our goal is to train a learning machine $g(\cdot)$ to estimate the fine-resolution radio map for all regions, i.e.,

$$\tilde{\mathbf{y}}_i = g(\mathcal{F}_i) \in \mathbb{R}_+^{256 \times 256}. \quad (6)$$

Unlike existing learning-based radio map reconstruction, we do not apply strict constraints on the distribution of samples and propagation model parameters. The following conditions are relaxed.

- 1) The sparse observations \mathbf{x}_i can be either uniformly or unevenly distributed over the whole region.
- 2) Different regions may have different number K_i of observations.
- 3) The transmitters in each region may have different radio propagation parameters.

To deal with such nonuniformly distributed observations and the unbalanced data samples over different training regions, we propose a two-phase learning framework for RME based on GAN, known as RME-GAN. Our goal is to train an efficient generator $g(\cdot)$ to estimate the full radio map as described in (6).

IV. RADIO MAP RECONSTRUCTION VIA RME-GAN

In this section, we present the design of the proposed RME-GAN, with the overall structure shown as Fig. 3. We first introduce the basic sketch of RME-GAN in Section IV-A, before describing the two-phase customization of features and loss functions in Sections IV-B and IV-C, respectively.

A. Sketch of RME-GAN

RME-GAN learns a mapping function $g(\cdot)$ from the region features \mathcal{F}_i to its output estimated full radio map $\tilde{\mathbf{y}}_i$. Since it is also a one-to-one mapping problem, we could design RME-GAN based on the general cGAN structure similar to Fig. 2. More specifically, we utilize an 18-layer deep Unet [12] structure for the sketch of the generator, with parameters shown in Table I.

To reformat the input features in \mathcal{F}_i , we first interpolate the sparse observations $(\mathbf{x}_i, \mathbf{c}_i)$ to the same size as region size via zero padding, i.e., $\mathbf{x}'_i \in \mathbb{R}_+^{256 \times 256}$. Since we consider a convolutional neural network (CNN) structure for Unet, the interpolated zeros would not influence other features. We then encode the transmitter locations \mathbf{P}_{ti} also in a 256×256 matrix \mathbf{p}_i , where the transmitter positions in \mathbf{p}_i are marked as 1 and other positions are 0. Features \mathcal{F}_i are encoded to three channels of features with size 256×256 , i.e., $\mathbf{f}_i = \{\mathbf{x}'_i, \mathbf{m}_i, \mathbf{p}_i\}$.

With the encoded features, the basic objective function of RME-GAN can be designed by

$$\begin{aligned} \min_{G} \max_{D} \quad V(D, G) &= \mathbb{E}_{\mathbf{y}, \mathbf{I} \sim p_{\text{data}}(\mathbf{y}, \mathbf{I})} [\log D(\mathbf{y}, \mathbf{I})] \\ &\quad + \mathbb{E}_{\mathbf{f} \sim p_{\text{data}}(\mathbf{f})} [\log (1 - D(G(\mathbf{f}), \mathbf{I}))] \end{aligned} \quad (7)$$

where $p_{\text{data}}(\mathbf{y}, \mathbf{I})$ is the joint distribution with the prior knowledge \mathbf{I} . More specifically, \mathbf{I} can be designed as a function of the region features, i.e., $\mathbf{I} = f(\mathcal{F}_i)$ or some determined labels, such as fake or real [38]. Here, we set $\mathbf{I} \in \mathbb{R}^{256 \times 256 \times 2}$ to represent the one-hot encodings in two-channel to give prior information to the discriminator as the input is a generated or real radio map.

We can split the min-max optimization problem into subproblems, and train the generator G and discriminator D iteratively. Specifically, the loss function to optimize D is

$$L_D = -V(D, G) \quad (8)$$

and the general loss function to optimize G is

$$L_G = \mathbb{E}_{\mathbf{x} \sim p_{\text{data}}(\mathbf{x})} [\log (1 - D(G(\mathbf{x}), \mathbf{I}))]. \quad (9)$$

The overall sketch of RME-GAN is illustrated in Fig. 3. Note that the cGAN can be customized by adding additional loss terms to capture desired properties. In this work, we consider a two-phase loss function design for (9) to capture the global and local information, respectively. More details will be discussed in Sections IV-B and IV-C.

TABLE I
STRUCTURE OF UNET

Layer	Input	1	2	3	4	5	6	7	8	9
Resolution	256	256	128	64	64	32	32	16	8	4
Channel	3	6	40	50	60	100	100	150	300	500
Filter	3	5	5	5	5	3	5	5	5	4
Layer	10	11	12	13	14	15	16	17	18	Output
Resolution	8	16	32	32	64	64	128	256	256	256
Channel	300+300	150+150	100+100	100+100	60+60	50+50	40+40	20+6+3	20+3	1
Filter	4	4	3	6	5	6	6	5	5	-

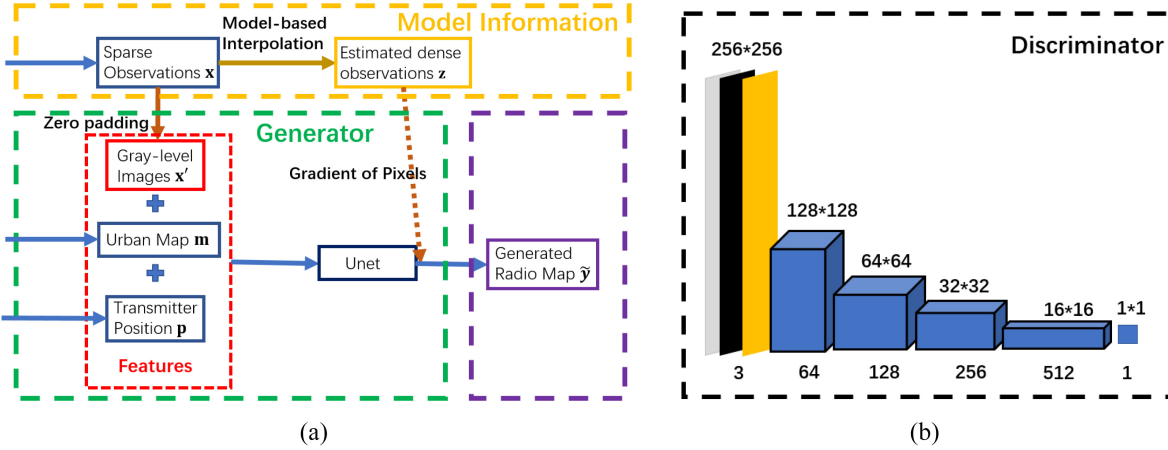


Fig. 3. Structure of RME-GAN: (a) generator takes input \mathcal{F}_i and consider the model information during training, where two phases of loss functions are applied to train the generator and (b) discriminator consists of four layers and generates a 1-D probability output. The discriminator input consists of three channels: the generated/true radio map (marked as orange), and the prior information as two-channel one-hot encodings (marked as gray and black).

B. Two-Phase Customization in RME-GAN

Earlier, we identified two challenges in RME: 1) how to efficiently integrate the radio propagation model with learning machines to capture global information and 2) how to estimate the details from biased and nonuniformly distributed observations. The first challenge lies in the estimation of global model information, while the second challenge deals with the shadowing effect and obstacle impact. To handle these challenges, we utilize different sampling strategies to extract global patterns and local features, respectively, as follows.

1) *Upsampling for Global Information*: In general, radio propagation should follow certain path-loss models, such as LDPL [8]. Thus, to model global path loss, we first upsample the sparse observations $(\mathbf{x}_i, \mathbf{c}_i)$ to a radio map template $\mathbf{z} \in \mathbb{R}_+^{256 \times 256}$ via model-based interpolation (MBI). Suppose that a system has N_t transmitter with positions (a_k, b_k) , $1 \leq k \leq N_t$. In MBI, the signal strength (in dB) at position (a, b) can be modeled as

$$P(a, b) = \sum_{k=1}^{N_t} \left(\alpha_k - 10\theta_k \log_{10} \left(\sqrt{(a_k - a)^2 + (b_k - b)^2} \right) \right) \quad (10)$$

where α_k is the power from the k th transmitter at the reference distance. Then, we optimize the parameters of the LDPL model from the observations by

$$\min_{\alpha_k, \theta_k} \sum_{j=1}^{K_i} (\mathbf{x}(j) - P(\mathbf{c}(j)))^2 \quad (11)$$

where $\mathbf{x}(j)$ is the j th observation with position $\mathbf{c}(j)$. By applying the LDPL model with estimated parameters, we can upsample the sparse observations \mathbf{x}_i as $\mathbf{z}_i \in \mathbb{R}_+^{256 \times 256}$.

Although MBI may be not able to capture the full effect of obstacles and shadowing, the upsampled template can still capture the global propagation pattern together with MBI model parameters. Consideration of upsampled features during the training process can provide a general guideline on radio map reconstruction. We introduce how to use \mathbf{z}_i to design loss functions of Phase 1 in Section IV-C.

2) *Downsampling for Detailed Features*: After estimating a template of reconstructed radio maps, we downsample the sparse observations in the second phase to correct errors in the details. We consider two downsampling strategies.

- 1) *Geometrywise Downsampling*: As discussed in Section III, sparse observations may be nonuniformly distributed over the whole space. To deal with unevenly distributed samples, we apply geometric information to downsample the observations. To balance the sample numbers in different locations, we first build superpixels [41] based on an urban map or interpolated template to split the entire region into N_s pieces. In each piece, we only pick one observation of peak energy. Then, we have a downsampled version of observations $\mathbf{x} \in \mathbb{R}_+^K$ as $\mathbf{x}_s \in \mathbb{R}_+^{N_s}$. In addition to superpixel-based space cut, other methods such as Voronoi diagram [8] or spectral clustering [42] can be also applied.

- 2) *Frequencywise Downsampling*: In digital signal processing, details and outliers are related to high frequencies in Fourier space. Thus, we could also transform the estimated radio map $\tilde{\mathbf{y}}$ to Fourier space as $\hat{\mathbf{y}}$. Then, we can select the first N_f Fourier coefficients in the high-frequency part as additional information in loss functions of the second phase, i.e., $\hat{\mathbf{y}}_f \in \mathbb{R}^{N_f}$.

With the extracted features under different sampling strategies, we propose a two-phase design on the loss functions for the training of the generator, i.e.,

$$L'_G = \begin{cases} L_G + L_{\text{Global}}, & \text{if } \epsilon < \tau \\ L_G + L_{\text{Local}}, & \text{if } \epsilon \geq \tau \end{cases} \quad (12)$$

where L_{Global} consist of loss functions favoring global model information and L_{Local} are the loss functions focusing on the local details. Here, a decision variable ϵ can be designed according to certain criteria, i.e., length of epochs or validation accuracy. For convenience, we keep a validation data set to evaluate the validation accuracy at each epoch to determine the phase change point. The specific design of loss functions will be introduced next in Section IV-C.

C. Loss Functions

After introducing the overall frameworks, we now present the design of loss functions.

- 1) *Phase 1—Global Model Prediction*: We first introduce the design of the loss function in the first phase.

- 1) *Baseline Loss Function*: The first term is the mean squared error (MSE) between the generated radio map and the ground truth \mathbf{y}

$$L_{\text{MSE}} = \frac{1}{256 \times 256} \cdot \|\mathbf{y} - \tilde{\mathbf{y}}\|_F^2 \quad (13)$$

where $\|\cdot\|_F$ is the Frobenius norm and $\tilde{\mathbf{y}} = g(\mathbf{f})$. We also consider a second term to be the total variation which describes the smoothness of the generated radio map [38]. More specifically, we apply the total variation of images

$$L_{\text{TV}} = \sum_{i,j \in \mathcal{N}} \|\tilde{\mathbf{y}}(i) - \tilde{\mathbf{y}}(j)\|_2^2 \quad (14)$$

where \mathcal{N} indicates pixel neighborhood and $\tilde{\mathbf{y}}(i)$ is the i th element of the estimated radio map $\tilde{\mathbf{y}}$.

- 2) *Loss Function of Global Information*: In addition to the baseline loss functions, we also utilize upsampled radio map \mathbf{z} from MBI to help the learning of global radio propagation patterns. Instead of directly evaluating the difference between $\tilde{\mathbf{y}}$ and \mathbf{z} , we focus on gradient patterns. Such gradient patterns feature the smoothness of radio propagation from transmitters to the surroundings. Since the first phase aims to learn the radio propagation model, MBI can help RME-GAN to learn the propagation model and speed up training. To obtain the gradient-based loss function, we first calculate the gradient of each pixel in the radio map for up, down, right, and left, i.e.,

$$\mathcal{G}(\tilde{\mathbf{y}}(i)) = [\mathcal{G}_{\text{up}}, \mathcal{G}_{\text{down}}, \mathcal{G}_{\text{right}}, \mathcal{G}_{\text{left}}] \in \mathbb{R}^4. \quad (15)$$

Then, we calculated the cosine similarity between $\mathcal{G}(\tilde{\mathbf{y}}(i))$ and $\mathcal{G}(\mathbf{z}(i))$. Then, the loss function of global information is defined as

$$L_{\text{Gradient}} = \sum_{i=1}^{256 \times 256} CS(\mathcal{G}(\tilde{\mathbf{y}}(i)), \mathcal{G}(\mathbf{z}(i))), \quad (16)$$

where $CS(\cdot)$ refers to the cosine similarity [43].

- 2) *Phase 2—Local Shadowing Estimation*: Next, we introduce the loss functions for local features in the second phase.

- 1) *Baseline Loss Function*: Similar to the first phase, the generated radio map should be smooth over the entire space. Thus, we also use total variation L_{TV} as one of the baseline loss functions. In addition, the L_{MSE} is also used here to control the overall accuracy. However, to emphasize more details depending on the downsampled observations, we assign a much smaller weight on L_{MSE} in the second phase compared to the first phase.

- 2) *Geometric Loss Function*: To mitigate the effect of nonuniformly distributed observations, we favor downsampled observations among all observations. Since the sparse observations are also true power gain in the radio map, we define a geometric loss function as the MSE between downsampled $\mathbf{x}_s = \mathbf{y}_s$ and the generated PSD at the same positions, denoted by $\tilde{\mathbf{y}}_s$, i.e.,

$$L_{\text{Geo}} = \text{MSE}(\mathbf{x}_s, \tilde{\mathbf{y}}_s). \quad (17)$$

- 3) *Frequency-Domain Loss Function*: As discussed before in Section IV-B, high-frequency coefficients in the Fourier space can capture the details or outliers in a radio map. To capture such information, we also calculate the MSE between $\hat{\mathbf{y}}_f$ and $\hat{\mathbf{y}}_f$ denoted by

$$L_{\text{HPF}} = \text{MSE}(\hat{\mathbf{y}}_f, \hat{\mathbf{y}}_f) \quad (18)$$

where $\hat{\mathbf{y}}_f$ includes the first top N_f high-frequency coefficients in the Fourier domain.

- 4) *Multiscale Structural Similarity Index (MS-SSIM)*: In image processing, the MS-SSIM is a useful term to evaluate the image quality based on the human visual system [44]. Since details in the radio map can be viewed as a fine-resolution image while the model-based template can be viewed as a coarse-resolution image, we could also consider the MS-SSIM index to improve the quality of generated radio map in the second phase. Let $\mathbf{u} = u_i | i = 1, 2, \dots, N$ and $\mathbf{v} = v_i | i = 1, 2, \dots, N$ be two discrete nonnegative signals, e.g., two image patches from the same position or two radio map residing on the same region. The luminance, contrast, and structure comparison measurements can be calculated as follows:

$$l(\mathbf{u}, \mathbf{v}) = \frac{2\mu_u\mu_v + C_1}{\mu_u^2 + \mu_v^2 + C_1} \quad (19)$$

$$c(\mathbf{u}, \mathbf{v}) = \frac{2\sigma_u\sigma_v + C_2}{\sigma_u^2 + \sigma_v^2 + C_2} \quad (20)$$

$$s(\mathbf{u}, \mathbf{v}) = \frac{2\sigma_{uv} + C_3}{\sigma_u\sigma_v + C_3} \quad (21)$$

where μ represents mean, σ is the variance, and C_i are small constants introduced in [45]. To calculate MS-SSIM, the system iteratively applies a low-pass filter and downsamples the filtered image by a factor of 2 on reference and distorted image signals as inputs. Suppose that M is the highest scale. The overall MS-SSIM is calculated by

$$\text{SSIM}(\mathbf{u}, \mathbf{v}) = [l_M(\mathbf{u}, \mathbf{v})]^{\alpha_M} \cdot \prod_{j=1}^M [c_j(\mathbf{u}, \mathbf{v})]^{\beta_j} [s_j(\mathbf{u}, \mathbf{v})]^{\gamma_j}. \quad (22)$$

Here, $\text{SSIM}(\mathbf{u}, \mathbf{v}) \leq 1$, and $\text{SSIM}(\mathbf{u}, \mathbf{v}) = 1$ iff $\mathbf{u} = \mathbf{v}$. The MS-SSIM loss function is defined by

$$L_{\text{SSIM}} = 1 - \text{SSIM}(\mathbf{y}, \tilde{\mathbf{y}}). \quad (23)$$

More properties of MS-SSIM can be found in [44].

D. Summary of Two-Phase Training Strategy

Combining all the loss terms aforementioned, the final loss function to train the generator is represented as

$$L'_G = \begin{cases} \lambda_1 L_G + \lambda_2 L_{\text{MSE}} + \lambda_3 L_{\text{TV}} + \lambda_4 L_{\text{Gradient}}, & \epsilon < \tau \\ \lambda_1 L_G + \lambda_2 L_{\text{MSE}} + \lambda_3 L_{\text{TV}} \\ + \lambda_5 L_{\text{SSIM}} + \lambda_6 L_{\text{Geo}} + \lambda_7 L_{\text{HPF}}, & \epsilon \geq \tau \end{cases}$$

where λ_i are the weights to control each loss term. In the first phase, we aim to apply MBI to help RME-GAN learn a template to capture the radio propagation model. After enough epochs, we favor more on the local information to correct errors in the details on the template by learning the shadowing effect and obstacle impact. Although some baseline loss functions are shared in both phases, the weights can be different depending on the specific tasks.

V. EXPERIMENTAL RESULTS

In this section, we present the experimental results of the proposed methods.

A. Experiment Setup

1) *Data Set*: In this work, we test the performance of the proposed method in the RadioMapSeer data set¹ [12]. The RadioMapSeer data set consists of 700 maps with 80 transmitter locations per map. The city maps are taken from OpenStreetMap [46] covering metropolitans such as Ankara, Berlin, Glasgow, Ljubljana, London, and Tel Aviv. The heights of the transmitters, receivers, and buildings are set to 1.5, 1.5, and 25 m, respectively, in this data set. The transmitter power equals 23 dBm and the carrier frequency is 5.9 GHz. The radio maps are generated using the software *WinProp* [47], and are saved in a 2-D grid of 256×256 m². The radio map has a 1-m resolution. More specifically, we test on the higher accuracy simulations in the RadioMapSeer data sets. An example of the RadioMapSeer data set is shown in Fig. 4, where building segmentation is considered as the urban map in our framework. The sparse observations are sampled from each radio map for training and testing.

¹<https://radiomapseer.github.io/>

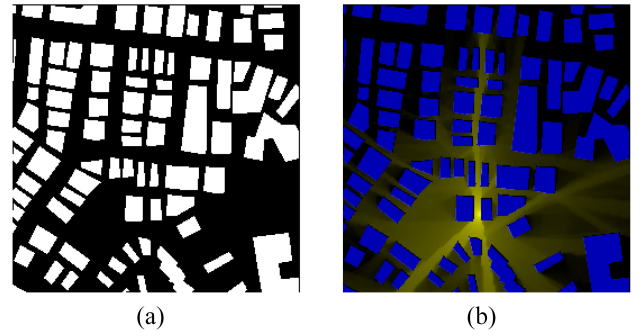


Fig. 4. Examples of RadioMapSeer data set: (a) urban maps with buildings as white and background as black and (b) radio map with path loss as yellow.

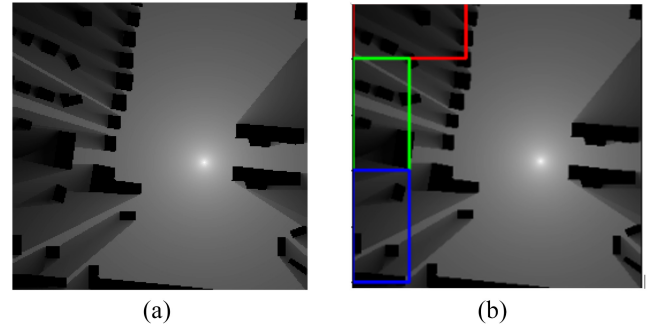


Fig. 5. One Example of radio map. (a) Ground truth. (b) Three selected regions.

2) *Data Splitting*: As mentioned in Section III, the sparse observations can be either uniformly or nonuniformly distributed over the whole space, and different regions may have a different number of observations. Thus, we sample the sparse observations under three different scenarios.

- 1) *Setup 1 (Uniformly Distributed)*: We uniformly sample 1% of sparse observations from the whole radio map.
- 2) *Setup 2 (Unbalanced Sample Distribution Among Regions)*: In this setup, we sample the radio map at a random ratio from 1% to 10% in each region, and the sparse observations are uniformly distributed.
- 3) *Setup 3 (Nonuniformly Distributed)*: We divide the radio map into two sides randomly. Then, we sample 1% of observations from one side and 10% from the other side.

We compare the proposed RME-GAN with other methods in all three scenarios to demonstrate its efficacy. The whole data set consists of 700 regions. For each experiment scenario, we split the data set with 500 regions as training data, 100 regions for testing, and 100 regions for validation.

3) *Parameters of Learning Models*: We utilize an 18-layer Unet for the generator with parameters shown in Table I, and a 4-layer discriminator shown as Fig. 3(b). In the first phase, the weights of each loss term are set as $\lambda_2 = 10$, $\lambda_3 = 0.01$, and $\lambda_4 = 1$. In the second phase, we set the weights as $\lambda_1 = 10$, $\lambda_2 = 1$, $\lambda_3 = 0.001$, $\lambda_4 = 0.0001$, $\lambda_5 = 0.0001$, and $\lambda_6 = 0.0001$. Note that, although both phases contain the L_{MSE} , λ_2 is set to be smaller in the second phase since we favor the downsampled radio map for the detail correction.

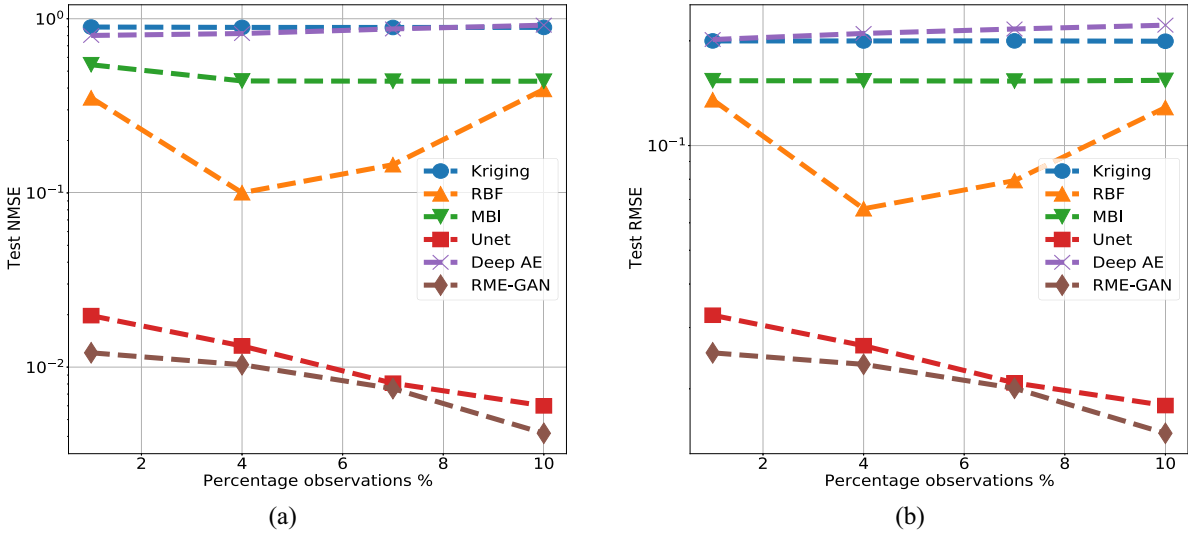


Fig. 6. Performance of different methods over different ratio of observations. (a) NMSE. (b) RMSE.

TABLE II
PERFORMANCE IN DIFFERENT SETUPS

Model	Setup 1		Setup 2		Setup 3	
	NMSE	RMSE	NMSE	RMSE	NMSE	RMSE
Kriging	0.8863	0.1947	0.8987	0.1962	0.9118	0.1971
RBF	0.3532	0.1343	0.1830	0.0884	0.3215	0.1295
MBI	0.8837	0.1973	0.5158	0.1499	0.5174	0.1500
cGAN	0.1559	0.0904	0.15077	0.0888	0.1506	0.0889
AE	0.1823	0.0978	0.2885	0.1238	0.2783	0.1217
Deep AE	0.1898	0.0998	0.3152	0.1295	0.3058	0.1274
Unet	0.0093	0.0220	0.0053	0.0166	0.0050	0.0161
RadioUnet	0.0052	0.0164	0.0042	0.0148	0.0046	0.0155
RME-GAN	0.0043	0.0151	0.0036	0.0130	0.0038	0.0140

B. Overall Accuracy

We first present the results in different setups. To evaluate the performance of the proposed RME-GAN, we compare it with the MBI interpolation [8], RBF interpolation [10], radioUnet [12], AE [14], deep AE [14], traditional Unet, Kriging interpolation [21], and traditional cGAN [36]. The normalized mean square error (NMSE) and root mean square error (RMSE) of the reconstructed radio map are present in Table II.

In Setup 1, samples are uniformly distributed. The learning-based approaches have better performance than the model-based and interpolation-based methods since the environment of these regions are more complex and the radio map is sensitive to the shadowing effect. Our RME-GAN outperforms all the methods in Setup 1. Especially, in comparison with traditional cGAN, our two-phase training process provides more information and displays superior performance. We also compare different methods over the different ratios of observations in Setup 1, shown in Fig. 6. Our proposed RME-GAN has the best performance results, as Table II further illustrates.

In Setup 2 and Setup 3, observations are biased among different regions and nonuniformly distributed, respectively. RME-GAN still shows the best results owing to the design of different sampling strategies. The experimental results

demonstrate the power of the proposed resampling methods and RME-GAN in radio map reconstruction.

Beyond the numerical results obtained, we also present the visualization results of a radio map in Fig. 5(a). The reconstructed results from different methods are shown in Fig. 7. Since interpolation-based methods, such as MBI and RBF cannot capture the impact of the environment efficiently, it fails to reconstruct the radio map in both three setups. Kriging-based methods provide a blurred construction of radio map as it estimates PSD from neighborhood data. Learning-based methods generally display better reconstruction. Compared to RadioUnet and AE, our RME-GAN constructs more accurate radio maps. Especially in view of Setup 3 where the sparse observations are nonuniformly distributed over the region, the proposed RME-GAN outperforms other existing learning methods. This happens because our resampling strategy is able to balance the samples over different locations. We also display the histogram of the reconstructed radio map in Setup 1 from RME-GAN as shown in Fig. 8, where RME-GAN is able to capture the distribution of PSD.

C. Robustness

1) *Two-Phase Training*: We first confirm the robustness of the two-phase training strategies. The validation error over time is shown in Fig. 9. From the results, the error drops when the training moves from Phase 1 to Phase 2, which indicates that the second phase could better correct detailed errors for the propagation template model from the first phase by leveraging the shadowing information.

2) *Zero-Shot Learning*: Zero-shot learning concerns the recognition of new concepts or new scenarios when a learning model is trained with generic data sets [48]. To evaluate the robustness and generalization of the proposed RME-GAN, we train the generator model by using data from Setup 1, but we

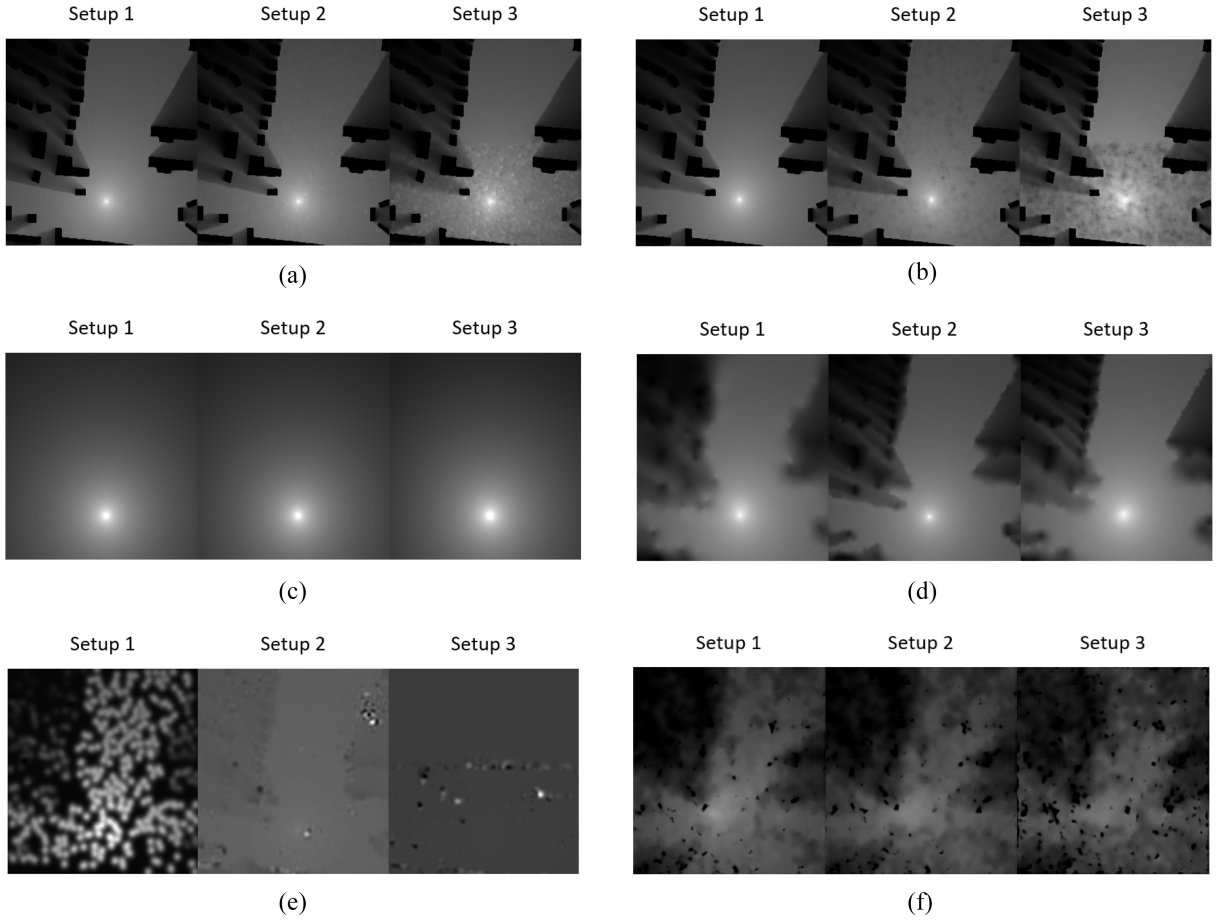


Fig. 7. Visualization results of different methods. (a) RME-GAN. (b) RadioUnet. (c) MBI. (d) Kriging. (e) RBF. (f) AE.

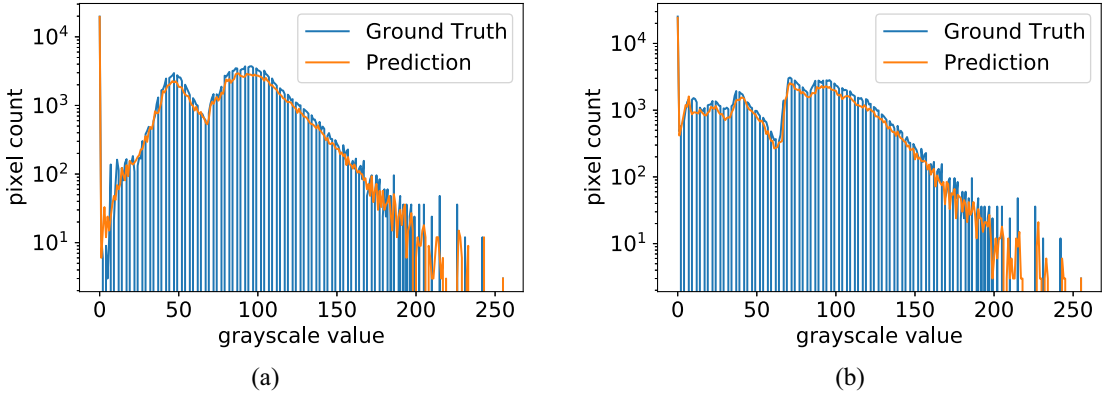


Fig. 8. One example of histograms of PSD in reconstructed radio maps. (a) Histogram in a training sample. (b) Histogram in a test sample.

test the performance in the data from Setup 2 and 3, respectively. The results are shown in Table III. From the results, we see that our RME-GAN can still obtain superior performance in the test data set with different distributions while other learning-based methods all observe a significant performance drop.

3) Performance in Areas With Lower Energy: Compared to the areas with larger energy, the areas with lower power spectra are more sensitive to the environment. To validate the performance of RME-GAN in areas with lower power,

we select three areas shown in Fig. 5(b) and test different methods in these three regions. The performance is shown in Table IV, where RME-GAN outperforms other methods in all areas and displays more robustness in the low-power areas.

D. Outage Fault Diagnosis

We perform outage analysis as a fault diagnosis. In some realistic applications, e.g., outage detection, we usually only need a coarse resolution of the radio map instead of a

TABLE III
PERFORMANCE OF ZERO-SHOT LEARNING

Model	Setup 2		Setup 3	
	NMSE	RMSE	NMSE	RMSE
cGAN	0.1613	0.0918	0.1984	0.1018
AE	0.2051	0.1038	0.2259	0.1094
Deep AE	0.1870	0.0991	0.1981	0.1019
Unet	0.0082	0.0208	0.0254	0.0367
RadioUnet	0.0052	0.0165	0.0148	0.0280
RME-GAN	0.0042	0.0150	0.0067	0.0190

TABLE IV
PERFORMANCE IN SELECTED AREAS

Model	Red Area		Green Area		Blue Area	
	RMSE	NMSE	RMSE	NMSE	RMSE	NMSE
RBF	0.0574	0.2794	0.0929	0.3317	0.0868	0.2803
Kriging	0.0675	0.3867	0.0890	0.3041	0.0819	0.2491
AE	0.0545	0.2518	0.0831	0.2651	0.0711	0.1879
MBI	0.1087	0.9520	0.1368	0.7183	0.0952	0.3372
cGAN	0.0449	0.1714	0.0723	0.2009	0.0466	0.0807
RadioUnet	0.0164	0.0228	0.0250	0.0240	0.0210	0.0163
RME-GAN	0.0151	0.0190	0.0221	0.0189	0.0172	0.0110

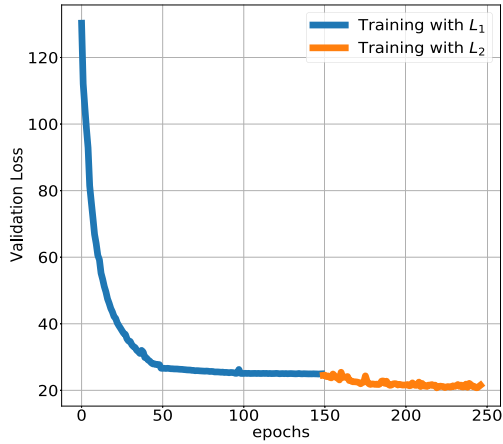


Fig. 9. Validation performance over different phase.

fine-resolution one. To evaluate the power of the proposed RME-GAN in reconstructing radio maps for such applications, we also compare the accuracy of the reconstructed outage maps. In our definition, a location experiences a power outage if its PSD falls below a preset threshold. Then, we can segment the radio map into an outage map with normal and outage areas, i.e., a binary segmentation. We compare the outage maps for all methods against two exemplary thresholds, i.e., 5 and 25. We measure performance by using segmentation errors in Table V. Moreover, we present the results of one randomly selected region, and the average of 10 randomly selected regions. Our proposed RME-GAN provides a more accurate outage map reconstruction compared to other approaches, which demonstrates the practicability of RME-GAN in network fault detection applications.

VI. CONCLUSION AND FUTURE DIRECTIONS

In this work, we propose a two-phase learning framework (RME-GAN) for the RME from sparse RF measurements.

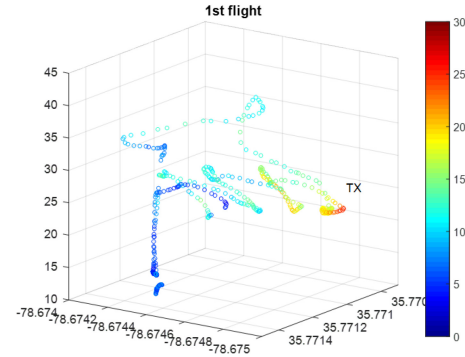


Fig. 10. Example of 3-D radio map reconstruction from the AERPAW platform.

TABLE V
OUTAGE EVALUATION (PREDICTION ERROR)

Model	Threshod = 5		Threshod = 25	
	Samples = 1	Average	Samples = 1	Average
RBF	0.1165	0.1265	0.2303	0.2349
MBI	0.1169	0.1391	0.1599	0.2359
Kriging	0.1870	0.0991	0.1381	0.1520
AE	0.1168	0.1525	0.1498	0.1586
RadioUnet	0.0085	0.0122	0.0144	0.0158
RME-GAN	0.0074	0.0105	0.0120	0.0141

Our RME-GAN first estimates a template to capture the global radio propagation patterns based on MBI. In the second phase, it learns the shadowing effects via geometric and frequency downsampling. The experimental results demonstrate the performance advantages and the robustness of the proposed RME-GAN, together with the two-phase training strategies in RME.

Rapid growth and broad deployment of IoT and 5G systems make efficient estimation and utilization of radio maps increasingly important. RMEs are valuable tools in resource allocation and network planning. From the perspective of IoT intelligence and edge AI [49], [50], we suggest some promising future directions as follows.

- One promising direction is the end-to-end learning frameworks of resource management for edge computation. From sparse spectrum measurements, one may study spectrum distribution and develop end-to-end data-driven approaches for specific network applications, such as fault diagnosis and dynamic wireless spectrum planning [51] as shown in Fig. 11.
- 3-D radio maps can serve as important tools for path planning of UAVs. Fig. 10 illustrates a case in which sparse spectrum observations may be gathered from UAVs in 3-D space. Efficient reconstruction of 3-D radio maps from sparse measurement can significantly benefit spectrum management and path planning for UAVs and other IoT devices requiring 3-D information.
- Federated learning [49] is a promising distributed computing framework to preserve data privacy. To improve Quality of Service (QoS) and to allow large-scale radio map reconstruction from different regions, integrating radio map reconstruction and federated learning poses

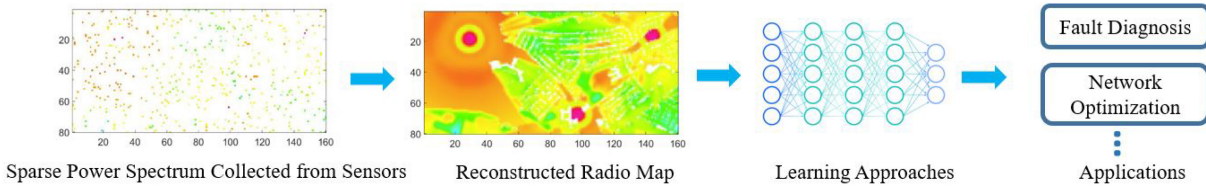


Fig. 11. Illustration of end-to-end frameworks for radio-map-assisted applications.

another interesting direction. For example, one urgent task is to enhance communication efficiency while preserving local data privacy.

- 4) Other practical directions include efficient compression of radio maps, radio map reconstruction for restricted areas, and estimation of interference maps.

We plan to explore these problems in our future works.

REFERENCES

- [1] Y. Deng et al., "Radio environment map construction using super-resolution imaging for intelligent transportation systems," *IEEE Access*, vol. 8, pp. 47272–47281, 2020.
- [2] S. Bi, J. Lyu, Z. Ding, and R. Zhang, "Engineering radio maps for wireless resource management," *IEEE Wireless Commun.*, vol. 26, no. 2, pp. 133–141, Apr. 2019.
- [3] S. Debroy, S. Bhattacharjee, and M. Chatterjee, "Spectrum map and its application in resource management in cognitive radio networks," *IEEE Trans. Cogn. Commun. Netw.*, vol. 1, no. 4, pp. 406–419, Dec. 2015.
- [4] S. Zhang and R. Zhang, "Radio map-based 3D path planning for cellular-connected UAV," *IEEE Trans. Wireless Commun.*, vol. 20, no. 3, pp. 1975–1989, Mar. 2021.
- [5] B. P. Nayak, L. Hota, A. Kumar, A. K. Turuk, and P. H. J. Chong, "Autonomous vehicles: Resource allocation, security, and data privacy," *IEEE Trans. Green Commun. Netw.*, vol. 6, no. 1, pp. 117–131, Mar. 2022.
- [6] Q. Liao, "SLAMORE: SLAM with object recognition for 3D radio environment reconstruction," in *Proc. IEEE Int. Conf. Commun. (ICC)*, Dublin, Ireland, Jun. 2020, pp. 1–7.
- [7] M. S. Riaz, H. N. Qureshi, U. Masood, A. Rizwan, A. Abu-Dayya, and A. Imran, "Deep learning-based framework for multi-fault diagnosis in self-healing cellular networks," in *Proc. IEEE Wireless Commun. Netw. Conf. (WCNC)*, Austin, TX, USA, May 2022, pp. 746–751.
- [8] M. Lee and D. Han, "Voronoi tessellation based interpolation method for Wi-Fi radio map construction," *IEEE Commun. Lett.*, vol. 16, no. 3, pp. 404–407, Mar. 2012.
- [9] J. A. Bazerque, G. Mateos, and G. B. Giannakis, "Group-Lasso on splines for spectrum cartography," *IEEE Trans. Signal Process.*, vol. 59, no. 10, pp. 4648–4663, Oct. 2011.
- [10] J. Krumm and J. Platt, "Minimizing calibration effort for an indoor 802.11 device location measurement system," Microsoft Res., Microsoft Corp., Redmond, WA, USA, Rep. MSR-TR-2003-82, Nov. 2003.
- [11] S.-P. Kuo and Y.-C. Tseng, "Discriminant minimization search for large-scale RF-based localization systems," *IEEE Trans. Mobile Comput.*, vol. 10, no. 2, pp. 291–304, Feb. 2011.
- [12] R. Levie, Ç. Yapar, G. Kutyniok, and G. Caire, "RadioUNet: Fast radio map estimation with convolutional neural networks," *IEEE Trans. Wireless Commun.*, vol. 20, no. 6, pp. 4001–4015, Jun. 2021.
- [13] O. Ronneberger, P. Fischer, and T. Brox, "U-net: Convolutional networks for biomedical image segmentation," in *Proc. Int. Conf. Med. Image Comput. Comput. Assist. Interv.*, Munich, Germany, Nov. 2015, pp. 234–241.
- [14] Y. Teganya and D. Romero, "Deep completion autoencoders for radio map estimation," *IEEE Trans. Wireless Commun.*, vol. 21, no. 3, pp. 1710–1724, Mar. 2022.
- [15] S. C. Beck, J. L. Turner, and O. Kovo, "High-resolution radio maps of Wolf-Rayet galaxies: Optically thick H II regions?" *Astron. J.*, vol. 120, no. 1, p. 244, Jul. 2000.
- [16] O. Esrafilian and D. Gesbert, "3D city map reconstruction from UAV-based radio measurements," in *Proc. GLOBECOM*, Singapore, Dec. 2017, pp. 1–6.
- [17] J. Johansson, W. A. Hapsari, S. Kelley, and G. Bodog, "Minimization of drive tests in 3GPP release 11," *IEEE Commun. Mag.*, vol. 50, no. 11, pp. 36–43, Nov. 2012.
- [18] M. Mirza and S. Osindero, "Conditional generative adversarial nets," 2014, *arXiv:1411.1784*.
- [19] X. Fu, N. D. Sidiropoulos, J. H. Tranter, and W.-K. Ma, "A factor analysis framework for power spectra separation and multiple emitter localization," *IEEE Trans. Signal Process.*, vol. 63, no. 24, pp. 6581–6594, Dec. 2015.
- [20] H. Braham, S. B. Jemaa, G. Fort, E. Moulines, and B. Sayrac, "Fixed rank Kriging for cellular coverage analysis," *IEEE Trans. Veh. Technol.*, vol. 66, no. 5, pp. 4212–4222, May 2017.
- [21] G. Boccolini, G. Hernández-Péñaloza, and B. Beferull-Lozano, "Wireless sensor network for spectrum cartography based on Kriging interpolation," in *Proc. IEEE 23rd Int. Symp. Pers. Indoor Mobile Radio Commun. (PIMRC)*, Sydney, NSW, Australia, Sep. 2012, pp. 1565–1570.
- [22] A. E. C. Redondi, "Radio map interpolation using graph signal processing," *IEEE Commun. Lett.*, vol. 22, no. 1, pp. 153–156, Jan. 2018.
- [23] X. Du, X. Liao, M. Liu, and Z. Gao, "CRCLoc: A crowdsourcing-based radio map construction method for WiFi fingerprinting localization," *IEEE Internet Things J.*, vol. 9, no. 14, pp. 12364–12377, Jul. 2022.
- [24] S. Zhang, T. Yu, J. Tivald, B. Choi, F. Ouyang, and Z. Ding, "Exemplar-based radio map reconstruction of missing areas using propagation priority," in *Proc. IEEE Global Commun. Conf.*, Rio de Janeiro, Brazil, Dec. 2022, pp. 1217–1222.
- [25] D. Schäufele, R. L. G. Cavalcante, and S. Stanczak, "Tensor completion for radio map reconstruction using low rank and smoothness," in *Proc. IEEE 20th Int. Workshop Signal Process. Adv. Wireless Commun. (SPAWC)*, Cannes, France, Jul. 2019, pp. 1–5.
- [26] C. Parera, Q. Liao, I. Malanchini, C. Tatino, A. E. C. Redondi, and M. Cesana, "Transfer learning for tilt-dependent radio map prediction," *IEEE Trans. Cogn. Commun. Netw.*, vol. 6, no. 2, pp. 829–843, Jun. 2020.
- [27] S. K. Vankayala, S. Kumar, I. Roy, D. Thirumulanathan, S. Yoon, and I. S. Kanakaraj, "Radio map estimation using a generative adversarial network and related business aspects," in *Proc. 24th Int. Symp. Wireless Pers. Multimedia Commun. (WPMC)*, Okayama, Japan, Feb. 2021, pp. 1–6.
- [28] C. Liu, H. Chang, and T. Park, "DA-cGAN: A framework for indoor radio design using a dimension-aware conditional generative adversarial network," in *Proc. IEEE/CVF Conf. Comput. Vis. Pattern Recognit. (CVPR) Workshops*, Jun. 2020, pp. 498–499.
- [29] H. Zou et al., "Adversarial learning-enabled automatic WiFi indoor radio map construction and adaptation with mobile robot," *IEEE Internet Things J.*, vol. 7, no. 8, pp. 6946–6954, Aug. 2020.
- [30] X. Wang, X. Wang, S. Mao, J. Zhang, S. C. G. Periaswamy, and J. Patton, "Indoor radio map construction and localization with deep Gaussian processes," *IEEE Internet Things J.*, vol. 7, no. 11, pp. 11238–11249, Nov. 2020.
- [31] Y. Zeng, X. Xu, S. Jin, and R. Zhang, "Simultaneous navigation and radio mapping for cellular-connected UAV with deep reinforcement learning," *IEEE Trans. Wireless Commun.*, vol. 20, no. 7, pp. 4205–4220, Jul. 2021.
- [32] K. Suto, S. Bannai, K. Sato, K. Inage, K. Adachi, and T. Fujii, "Image-driven spatial interpolation with deep learning for radio map construction," *IEEE Wireless Commun. Lett.*, vol. 10, no. 6, pp. 1222–1226, Jun. 2021.
- [33] H. J. Bae and L. Choi, "Large-scale indoor positioning using geomagnetic field with deep neural networks," in *Proc. IEEE Int. Conf. Commun. (ICC)*, Shanghai, China, May 2019, pp. 1–6.

- [34] T. Imai, K. Kitao, and M. Inomata, "Radio propagation prediction model using convolutional neural networks by deep learning," in *Proc. 13th Eur. Conf. Antennas Propag. (EuCAP)*, Krakow, Poland, Jun. 2019, pp. 1–5.
- [35] D. Romero and S.-J. Kim, "Radio map estimation: A data-driven approach to spectrum cartography," *IEEE Signal Process. Mag.*, vol. 39, no. 6, pp. 53–72, Nov. 2022.
- [36] I. Goodfellow et al., "Generative adversarial networks," *Commun. ACM*, vol. 63, pp. 139–144, Nov. 2020.
- [37] D. Pathak, P. Krahenbuhl, J. Donahue, T. Darrell, and A. A. Efros, "Context encoders: Feature learning by inpainting," in *Proc. IEEE Conf. Comput. Vis. Pattern Recognit.*, Las Vegas, NV, USA, Jun. 2016, pp. 2536–2544.
- [38] Y. Liu, Z. Qin, T. Wan, and Z. Luo, "Auto-painter: Cartoon image generation from sketch by using conditional Wasserstein generative adversarial networks," *Neurocomputing*, vol. 311, pp. 78–87, Oct. 2018.
- [39] P. Isola, J.-Y. Zhu, T. Zhou, and A. A. Efros, "Image-to-image translation with conditional adversarial networks," in *Proc. IEEE Conf. Comput. Vis. Pattern Recognit.*, Honolulu, HI, USA, Jul. 2017, pp. 1125–1134.
- [40] T.-C. Wang, M.-Y. Liu, J.-Y. Zhu, A. Tao, J. Kautz, and B. Catanzaro, "High-resolution image synthesis and semantic manipulation with conditional GANs," in *Proc. IEEE Conf. Comput. Vis. Pattern Recognit.*, Salt Lake City, UT, USA, Jun. 2018, pp. 8798–8807.
- [41] S. Zhang, Q. Deng, and Z. Ding, "Multilayer graph spectral analysis for hyperspectral images," *EURASIP J. Adv. Signal Process.*, vol. 1, no. 92, pp. 1–25, Oct. 2022.
- [42] S. Zhang, Z. Ding, and S. Cui, "Introducing hypergraph signal processing: Theoretical foundation and practical applications," *IEEE Internet Things J.*, vol. 7, no. 1, pp. 639–660, Jan. 2020.
- [43] H. V. Nguyen and L. Bai, "Cosine similarity metric learning for face verification," in *Proc. Asian Conf. Comput. Vis.*, Queenstown, New Zealand, Nov. 2010, pp. 709–720.
- [44] Z. Wang, E. P. Simoncelli, and A. C. Bovik, "Multiscale structural similarity for image quality assessment," in *Proc. 37th Asilomar Conf. Signals Syst. Comput.*, Pacific Grove, CA, USA, Nov. 2003, pp. 1398–1402.
- [45] Z. Wang, A. C. Bovik, H. R. Sheikh, and E. P. Simoncelli, "Image quality assessment: From error visibility to structural similarity," *IEEE Trans. Image Process.*, vol. 13, pp. 600–612, 2004.
- [46] "OpenStreetMap contributors." Planet Dump. 2017. [Online]. Available: <https://planet.osm.org>
- [47] R. Hoppe, G. Wolfe, and U. Jakobus, "Wave propagation and radio network planning software WinProp added to the electromagnetic solver package FEKO," in *Proc. Int. Appl. Comput. Electromagn. Soc. Symp. Italy (ACES)*, Florence, Italy, Mar. 2017, pp. 1–2.
- [48] B. R. Paredes and P. Torr, "An embarrassingly simple approach to zero-shot learning," in *Proc. Int. Conf. Mach. Learn.*, Lille, France, Jun. 2015, pp. 2152–2161.
- [49] R. Singh and S. S. Gill, "Edge AI: A survey," *Internet Things Cyber-Phys. Syst.*, vol. 3, pp. 71–92, Mar. 2023.
- [50] S. Iftikhar et al., "AI-based fog and edge computing: A systematic review, taxonomy and future directions," *Internet Things*, vol. 21, Apr. 2023, Art. no. 100674.
- [51] M. G. Kibria, K. Nguyen, G. P. Villardi, O. Zhao, K. Ishizu, and F. Kojima, "Big data analytics, machine learning, and artificial intelligence in next-generation wireless networks," *IEEE Access*, vol. 6, pp. 32328–32338, 2018.



Songyang Zhang received the Ph.D. degree in electrical and computer engineering from the University of California at Davis, Davis, CA, USA, in 2021.

He is currently a Postdoctoral Research Associate with the Department of Electrical and Computer Engineering, University of California at Davis. His current research interests include signal processing and learning over high-dimensional graphs, federated learning, biomedical signal processing, and wireless network optimization.



Achintha Wijesinghe received the bachelor's degree in electronic and telecommunication engineering from the University of Moratuwa, Moratuwa, Sri Lanka, in 2020. He is currently pursuing the Ph.D. degree with the Department of Electrical and Computer Engineering, University of California at Davis, Davis, CA, USA.

His research interests include federated learning, distributed learning, computer vision, and algorithm development.



Zhi Ding (Fellow, IEEE) received the Ph.D. degree in electrical engineering from Cornell University, Ithaca, NY, USA, in 1990.

From 1990 to 2000, he was a Faculty Member with Auburn University, Auburn, AL, USA, and later, University of Iowa, Iowa, IA, USA. He joined the College of Engineering, University of California at Davis, Davis, CA, USA, in 2000, where he is with the Department of Electrical and Computer Engineering and holds the position of a Distinguished Professor. He has coauthored the textbook: *Modern Digital and Analog Communication Systems* 5th edition, (Oxford University Press, 2019). His major research interests and expertise cover the areas of wireless networking, communications, signal processing, multimedia, and learning.

Prof. Ding received the IEEE Communication Society's WTC Award in 2012 and the IEEE Communication Society's Education Award in 2020. He was the General Chair of the 2016 IEEE International Conference on Acoustics, Speech, and Signal Processing and the Technical Program Chair of the 2006 IEEE Globecom. He was also an IEEE Distinguished Lecturer (Circuits and Systems Society from 2004 to 2006, Communications Society from 2008 to 2009. He served as an IEEE TRANSACTIONS ON WIRELESS COMMUNICATIONS Steering Committee Member from 2007 to 2009 and its Chair from 2009 to 2010. He was an Associate Editor of the IEEE TRANSACTIONS ON SIGNAL PROCESSING from 1994 to 1997 and from 2001 to 2004 and IEEE SIGNAL PROCESSING LETTERS from 2002 to 2005. He has served as the Chief Information Officer and Chief Marketing Officer for the IEEE Communications Society. He was a member of the Technical Committee on Statistical Signal and Array Processing and Technical Committee on Signal Processing for Communications from 1994 to 2003.